# The Star-Forming Main Sequence and the contribution of dust-obscured star formation over the last 12 Gyrs from the FUV+IR luminosity functions

ALDO RODRÍGUEZ-PUEBLA , VLADIMIR AVILA-REESE , MARIANA CANO-DÍAZ , S. M. FABER, JOEL R. PRIMACK, JOSÉ FRANCO, I. ARETXAGA, AND EDER SANTIAGO-MAYORAL

<sup>1</sup> Instituto de Astronomía Universidad Nacional Autónoma de México, A. P. 70-264, 04510, México, D.F., México
 <sup>2</sup> CONACYT Research fellow - Instituto de Astronomía Universidad Nacional Autónoma de México, A. P. 70-264, 04510, México, D.F., México

<sup>3</sup> UCO/Lick Observatory, Department of Astronomy and Astrophysics, University of California, Santa Cruz, CA 95064, USA
<sup>4</sup> Physics Department, University of California, Santa Cruz, CA 95064, USA

### Submitted to ApJ

### ABSTRACT

We use a statistical approach to study the evolution of the star-forming galaxy (SFG) main sequence (MS) and the fraction of dust-obscured star formation up to  $z \sim 4$ . We use the following observables: the far-ultraviolet, FUV, and the infrared, IR, luminosity functions, LFs, and the galaxy stellar mass function (GSMF) of SFGs. Our derived total (FUV+IR) star formation rates, SFR, reproduce the evolution of the MS as compared to a set of independent observational inferences. At any redshift, we find that the specific SFR- $M_*$  relation for MS SFGs approaches to a power law at the high-mass end. At lower masses it bends and eventually the slope sign changes from negative to positive at very low masses. At  $z \sim 0$ , this change of sign is at  $M_* \sim 5 \times 10^8 \rm M_{\odot}$  close to dust-obscured star formation regime,  $M_* \sim 6 \times 10^8 {\rm M}_{\odot}$ . The slope sign change is related to the knee of the FUV LF. We predict that the assembly time of nearby dwarf galaxies is  $\sim 10$  Gyrs consistent with their oldest observed stellar populations. Our derived dust-obscured fractions agree with previous determinations at  $0 \le z \le 2.5$ . The dust-obscured fraction depends strongly on mass with almost no dependence with redshift above  $z \sim 1.2$ . At  $z \lesssim 0.75$  high-mass galaxies become more "transparent" compared to their high redshift counterparts. On the opposite, low- and intermediate-mass galaxies have become more obscured by dust. Using the joint evolution of the GSMF and the FUV and IR LFs is a promising empirical approach to study the stellar mass growth and dust formation/destruction mechanisms, and ultimately to constrain galaxy formation models.

Keywords: galaxies: star formation — galaxies: luminosity function, mass function — galaxies: statistics — galaxies: evolution — (ISM:) dust, extinction

### 1. INTRODUCTION

Over the last two decades, major advances have occurred in assembling large galaxy samples from multiwavelength imaging surveys. Now the properties of galaxies are studied with unprecedented accuracy in statistical representative samples of both local and distant galaxies. This has led to tremendous progress in improv-

Corresponding author: Aldo Rodríguez-Puebla apuebla@astro.unam.mx

ing our observational understanding on the evolution of the galaxy stellar mass function (GSMF, for recent discussions and compilations of observations up to high redshifts, see Conselice et al. 2016; Rodríguez-Puebla et al. 2017), as well as the evolution of the star formation rate, SFR, as a function of stellar mass  $M_*$  (SFRs, see e.g., Speagle et al. 2014; Rodríguez-Puebla et al. 2017) and the cosmic star formation history (Madau & Dickinson 2014; Driver et al. 2018).

With the above observational advances, the relationship between the SFR and the  $M_*$  has received an intense scrutiny by many authors over the last years.

<sup>&</sup>lt;sup>5</sup> Instituto Nacional de Astrofísica, Óptica y Electrónica (INAOE), Aptdo. Postal 51 y 216, 72000 Puebla, Pue., México

In particular, there is a class of star-forming galaxies, SFGs, that are known to obey a tight SFR- $M_*$  relation,  $\sim 0.3$  dex of scatter, and establishing what in the literature has been coined as "Main-Sequence" (MS, Brinchmann et al. 2004; Noeske et al. 2007; Salim et al. 2007, for more recent studies and reviews see Speagle et al. 2014; Whitaker et al. 2014; Santini et al. 2017). The tightness of this relation and the abundance of galaxies in the MS, reflects that most galaxies spend a considerable time building their stars in an approximately self-regulated way within this sequence (see e.g., Bouché et al. 2010; Davé et al. 2012), hence its importance for galaxy formation. Starburst galaxies are another class of SFGs with elevated amounts of star formation, typically associated with galaxy mergers, that are outliers of the MS but represent only a few percent ( $\sim 10-15\%$ ) of the total population (Rodighiero et al. 2011; Sargent et al. 2012). Quenched galaxies are another class of galaxies that are off the MS, in this case due their low levels of star formation (e.g., Wuyts et al. 2007; Williams et al. 2009); their fraction has increased rapidly since  $z \lesssim 2$ (Muzzin et al. 2013). In this paper we focus on MS SFGs.

Considering these now well-established findings there are yet some open questions with respect to the distribution of the SFRs of SFGs. Does the SFR- $M_*$  relationship extend to low-mass galaxies and dwarfs,  $M_* \lesssim 10^9 {\rm M}_{\odot}$ , with the same slope as intermediate- and high-mass galaxies? What is the contribution from dust-obscured star formation as a function of stellar mass and redshift?

This paper addresses the above questions by using the redshift evolution of the far-ultraviolet FUV (1500Å) and the total infrared, IR (8 – 1000 $\mu$ m) rest-frame luminosity functions, LFs, combined with the evolution of the GSMF of SFGs. While the above questions have been investigated separately by some authors in the past (e.g., McGaugh et al. 2017 and Davies et al. 2019 studied the SFR- $M_*$  relation at low masses while Whitaker et al. 2017 studied the contributions from dust-obscured star formation), it is important and timely to address the above two questions at the same time as well as their possible physical correlations and implications for galaxy formation models. Moreover, we note that the joint evolution of the GSMF and the FUV and IR rest-frame luminosity functions has not yet received atten-

tion in the light of the above questions. The novelty of using the joint evolution of the GSMF and the FUV and IR LFs is that it offers a new way to derive and study the SFR- $M_{\ast}$  relationship and its decomposition into the unobscured and obscured contributions. One of the main implications of this paper is that together these three distributions offer a powerful tool that contributes to the study of the emergence of the galaxy mass distributions, stellar mass growth and dust formation/destruction, and ultimately to constrain galaxy formation models.

This paper is divided into four sections. The statistical method we employed to link  $M_*$  to SFR is introduced in Section 2. Section 3 presents our results and compares to a set of independent observations finding a good agreement between them. This suggest that our approach represents a new powerful and novel tool to study at the same time the redshift evolution of MS SFGs and the dependence of the fraction of dust-obscured star formation with stellar mass. Finally, in Section 4 we summarize and discuss our results.

In this paper we adopt the following cosmological parameter values:  $\Omega_{\Lambda} = 0.7$ ,  $\Omega_{\rm m} = 0.3$ , and h = 0.7. All stellar masses are normalized to a Chabrier (2003) Initial Mass Function, IMF.

### 2. MODELING THE FUV+IR SFR DISTRIBUTIONS

Here we present a new statistical approach to derive the redshift evolution of the conditional distribution of SFR given  $M_*$  for MS galaxies and all its moments. In particular, our main aim is the derivation of the redshift evolution of the mean SFR- $M_*$  relationship for MS galaxies. Normally, the evolution of the MS is inferred by combining galaxy samples at different redshifts for which the SFRs are estimated for every galaxy (e.g., Whitaker et al. 2014; Salim et al. 2016). At this point, it should be said that (i) galaxy samples are subject to (their own) selection effects, and (ii) the SFRs reported by different authors are based on different tracers and methods. As a result, the derived SFR- $M_*$  relation and its evolution will be biased. On the other hand, the comparison of the SFR- $M_*$  relation and its evolution estimated by different ways is not trivial, though some authors have attempted to homogenize different determinations (see e.g., Speagle et al. 2014; Rodríguez-

<sup>&</sup>lt;sup>1</sup> There are notable studies that have combined some of them but not all of them at the same time. For example, Béthermin et al. (2012) used the IR LF and the GSMF while Burgarella et al. (2013) used the FUV and IR. More recently Tacchella et al. (2018) used the FUV to study the distribution of SFRs.

Puebla et al. 2017). Thus, to infer robust relations, specially for constraining accurately the shape of the MS in a *broad mass* and *redshift* ranges, the optimal is to use a homogeneous method to calculate the SFRs from galaxy samples for which the volume completeness is well established. This is the case of our approach.

As mentioned earlier, the novelty of our approach is that it combines observational FUV and IR rest-frame LFs at different redshifts with the GSMFs of SFGs to derive the mean SFR– $M_{\ast}$  relationship and its scatter over a broad mass and redshift range. The advantage of this approach is that it uses a uniform way to determine the SFRs at all redshifts and the sample completeness above given limits is well controlled.

Following, we describe how we constrain the conditional distribution of SFR given  $M_*$  when combining the FUV and IR LFs and the GSMF of SFGs at different redshifts. The conditional distributions allows to compute any moment, in particular the first moment, that is, the mean SFR- $M_*$  relationship. Notice that our method naturally separates the SFRs into their unobscured and dust-obscured components, allowing this to study the dust-obscured fraction at the same time.

#### 2.1. The conditional SFR distributions

Motivated by observations, we assume that the MS is a non decreasing relation between  $M_*$  and SFR. The key assumption in our approach is that the convolution between the conditional distributions of SFR given  $M_*$  and the observed GSMF of SFGs maps into the FUV and IR rest-frame LFs. In other words, we are assuming that the FUV and IR LFs emerged from the MS galaxy population. This is actually inaccurate in the case of the IR LF as starburst galaxies also contribute to the LF (see e.g., Sargent et al. 2012; Gruppioni et al. 2013). Fortunately, their contribution becomes relatively important only at the high luminosity end and this contribution can be estimated. Following the results presented in Sargent et al. (2012), we assume that the IR-based SFR distribution is composed by the contributions of both MS and starburst galaxies. Next, we will discuss the conditional SFR distributions given  $M_*$  and their moments. While all the quantities that we discuss below depend on redshift, we do not show this dependence for simplicity.

We begin by introducing the conditional lognormal distribution  $\mathcal{N}(y|x)$  given by:

$$\mathcal{N}(y|x)d\log y = \frac{d\log y}{\sqrt{2\pi\sigma_y^2}} \exp\left[-\frac{(\log y - \mu(x))^2}{2\sigma_y^2}\right], \quad (1)$$

where the mean is  $\mu(x) = \langle \log y(x) \rangle$ , and  $\sigma_y$  is the logarithmic width of the distribution, referred here as its

scatter. Since we will work in a space in which the logarithm of y is lognormal distributed, for simplicity, we will refer sometimes to  $\langle \log y(x) \rangle$  as the mean y-x relation. In some cases authors report  $\langle y \rangle$ ; for a lognormal distribution the offset between  $\langle \log y \rangle$  and  $\langle y \rangle$  is given by (see e.g., Rodríguez-Puebla et al. 2017):

$$\log\langle y\rangle = \langle \log y\rangle + \frac{\sigma^2}{2}\ln 10. \tag{2}$$

We define the conditional probability distribution of SFRs given a stellar mass as  $\mathcal{P}_{\psi,X}(\mathrm{SFR}_X|M_*)$ , where X refers to the SFRs computed based on the FUV or IR rest-frame luminosities. In the case of SFR<sub>FUV</sub>, we assume that  $\mathcal{P}_{\psi,\mathrm{FUV}} = \mathcal{N}(\mu_{\mathrm{FUV}},\sigma_{\mathrm{FUV}})$  with a scatter  $\sigma_{\mathrm{FUV}}$  independent of  $M_*$  and mean  $\mu_{\mathrm{FUV}} = \langle \log \mathrm{SFR}_{\mathrm{FUV}}(M_*) \rangle$ . As for the distribution of SFR<sub>IR</sub>, as mentioned above, it is composed by the contributions of MS and starburst galaxies. Therefore,

$$\mathcal{P}_{\psi,IR} = (1 - \mathcal{A}_{SB}) \times \mathcal{P}_{\psi,IR-MS} + \mathcal{A}_{SB} \times \mathcal{P}_{\psi,IR-SB},$$

where  $\mathcal{A}_{SB}$  is the fraction of starburst galaxies at fixed stellar mass, and the conditional distributions  $\mathcal{P}_{\psi,\mathrm{IR-MS}}$  and  $\mathcal{P}_{\psi,\mathrm{IR-SB}}$  are lognormal distributed (Eq. 1). Following Sargent et al. (2012), we assume that  $\sigma_{\mathrm{IR}}(=\sigma_{\mathrm{IR-SB}}=\sigma_{\mathrm{IR-MS}})$  and  $\mathcal{A}_{SB}$  are both independent of mass and that  $\mu_{\mathrm{IR-SB}}=\mu_{\mathrm{IR-MS}}+\mu_0$ , where  $\mu_{\mathrm{IR-MS}}=\langle\log\mathrm{SFR}_{\mathrm{IR-MS}}(M_*)\rangle$  is the mean relation for the MS galaxies (hereafter we will refer to it just as  $\langle\log\mathrm{SFR}_{\mathrm{IR}}\rangle$ ). Based on the recent results from Schreiber et al. (2015) we use  $\mathcal{A}_{SB}=0.033$  and  $\mu_0=0.79$ .

As for the scatters  $\sigma_{FUV}$  and  $\sigma_{IR}$ , first note that observations based on mass-complete samples have shown that the scatter around the SFR- $M_*$  relationship is of the order of 0.3 dex (Speagle et al. 2014; Schreiber et al. 2015; Cano-Díaz et al. 2016; Fang et al. 2018). Nonetheless, recent results have shown that the scatter could increase up to  $\sim 0.4$  dex at the high mass end (Ilbert et al. 2015; Popesso et al. 2019a,b). While the discussion of the real trends and values of the MS scatter is beyond the scope of this paper, here we assume a constant scatter of  $\sigma_{\rm FUV} = 0.3$  dex for the FUV and  $\sigma_{\rm IR} = 0.4$ for the IR and zero covariance between the two distributions. The above will lead to a scatter around the inferred mean SFR- $M_*$  relations that has some dependence on  $M_*$  (see Equation 7 described below), in the direction that for low mass galaxies,  $\sigma \sim 0.3$  dex while for massive galaxies,  $\sigma \sim 0.4$  dex.

 $<sup>^2</sup>$  Note that this value differs from the one reported in Schreiber et al. (2015). The reason for this is that we are taking into account that the distribution of their SFGs is not centred in  $R_{\rm SB}=1$ , the starburstiness parameter defined by the authors, see their best fit models to their equation 10 and figure 19.

As for the mean  $\langle \log \mathrm{SFR_{FUV}}(M_*) \rangle$  and  $\langle \log \mathrm{SFR_{IR}}(M_*) \rangle$  relations we now describe our proposed parametric functions. To our knowledge there are not parametric functions previously reported in the literature for these relations. We proposed our parametric functions by noticing that the generic shapes of the  $\mathrm{SFR_{FUV}}{-}M_*$  and  $\mathrm{SFR_{IR}}{-}M_*$  relations are governed by the shape of their corresponding FUV and IR LFs. For the mean  $\mathrm{SFR_{FUV}}{-}M_*$  relation, we assume a double power law (defined by four parameters):

$$\langle \log SFR_{FUV}(M_*) \rangle = \mu_{FUV,0} + \log \left( \frac{2}{\left(\frac{M_*}{M'_{FUV}}\right)^{\alpha} + \left(\frac{M_*}{M'_{FUV}}\right)^{\beta}} \right),$$
(3)

while for the mean  $SFR_{IR}-M_*$  we assume a Gompertz-like function that dominates at the low mass end and a power-law that dominates at the high mass end (defined by three parameters):

$$\langle \log \mathrm{SFR}_{\mathrm{IR}}(M_*) \rangle = \mu_{\mathrm{IR},0} + \log \left( \frac{(M_*/M'_{\mathrm{IR}})^{\gamma}}{\exp\left(-e^{-\log(M_*/M'_{\mathrm{IR}})}\right)} \right). \tag{4}$$

Notice that all the parameters from the above equations depend on redshift. In Section 2.3 we discuss the functions that we use for the dependences with redshift and their corresponding best fitting parameters to the observational data through our statistical approach.

The final step for characterizing the total conditional SFR distribution given  $M_*$  for galaxies in the MS is given by the combination of both the FUV- and IR-based conditional SFR distributions described above. The total SFR distribution is:

$$\mathcal{P}_{\psi}(\text{SFR}|M_{*}) = \int \frac{\mathcal{P}_{\psi,\text{FUV}}(\text{SFR} - \text{SFR}_{\text{IR}}|M_{*})}{1 - \text{SFR}_{\text{IR}}/\text{SFR}} \times \frac{1}{(5)}$$

$$\mathcal{P}_{\psi,\text{IR}-\text{MS}}(\text{SFR}_{\text{IR}}|M_{*})d\log\text{SFR}_{\text{IR}}.$$

Note that for the IR SFR distribution we use only the component of MS galaxies. A few words on the above distribution are worth mentioning at this point. While the sum of normally distributed random variables is also normally distributed, this is not the case for lognormal distributed random variables. To our knowledge there is not an analytical solution for lognormal distributions, so this is computed numerically via Equation (5). From the above equation we can derive the total mean (hereafter we will refer sometimes to it as simply the mean) SFR– $M_*$  relation:

$$\langle \log \text{SFR}(M_*) \rangle = \int \log \text{SFR} \, \mathcal{P}_{\psi}(\text{SFR}|M_*) d \log \text{SFR}.$$
 (6)

The scatter around the mean is

$$\sigma_{\rm SFR}^2(M_*) = \int (\log {\rm SFR} - \langle \log {\rm SFR}(M_*) \rangle)^2 \times \mathcal{P}_{\psi}({\rm SFR}|M_*) d \log {\rm SFR}.$$
 (7)

We will also report the mean  $\langle \log \mathrm{sSFR}(M_*) \rangle$  relation with  $\mathrm{sSFR} = \mathrm{SFR}/M_*$  and  $\sigma_{\mathrm{sSFR}} = \sigma_{\mathrm{SFR}}$ . Since we use separately the observations of the IR and FUV LFs, a straightforward outcome from our approach is the determination of the separate contributions from FUV and IR to the total SFRs. This will be important for deriving the dust-obscured fraction as a function of mass and redshift.

### 2.2. The FUV and IR LFs

In this section we describe how the FUV and IR LFs are derived by convolving the GSMF of SFGs and the conditional FUV and IR SFR probability distributions. For the above, we begin by using the Kennicutt (1998) conversion factors,  $\mathcal{K}_X$ , to transform SFRs into luminosities, that is,  $L_X = \mathcal{K}_X/\text{SFR}_X$ . These conversion factors allow us to pass from the SFR conditional probability distributions,  $\mathcal{P}_{\psi,X}(\text{SFR}_X|M_*)$ , to the respective distributions of luminosities:  $\mathcal{P}_{l,X}(L_X|M_*)$ . Then the LF of the FUV and IR light is related to the GSMF of SFGs,  $\phi_{\text{SF},a}$ , by the following convolution:

$$\phi_X(L_X) = \int \mathcal{P}_{l,X}(L_X|M_*)\phi_{SF,g}(M_*)d\log M_*.$$
 (8)

For the GSMF of SFGs we use the best fitting model to the compiled GSMF data from Rodríguez-Puebla et al. (2017) and their reported evolution of the fraction of SFGs as a function of  $M_*$  (for details see Appendix A ). We note that the above integral is not computed from  $M_* = 0$  but from  $M_* = 10^6 {\rm M}_{\odot}$ , which is yet  $\sim 1-1.5$  dex below the observational limit of our GSMFs.

The observational LFs are actually reported over redshift intervals,  $z_i < z < z_f$ . We take into account the above by using the following equation:

$$\phi_{\text{obs},X}(L_X; z_i, z_f) = \frac{\int_{z_i}^{z_f} \phi_X(L_X, z) dV}{V(z_f) - V(z_i)},$$
(9)

where V is the comoving volume.

The original Kennicutt (1998) conversion factors were obtained on the assumption of a Salpeter (1955) IMF.<sup>3</sup> According to Madau & Dickinson (2014), we multiply the original conversion factors by 0.63 to convert them into a Chabrier (2003) IMF: the FUV conversion factor changes to  $\mathcal{K}_{\rm FUV}=1.7\times 10^{-10}{\rm M}_{\odot}~{\rm yr}^{-1}L_{\odot}^{-1}$ , while the IR factor changes to  $\mathcal{K}_{\rm IR}=1.09\times 10^{-10}{\rm M}_{\odot}~{\rm yr}^{-1}L_{\odot}^{-1}$ . Notice that the FUV light refers to the observed luminosity, which can be obscured in the presence of dust. In the following, we assume that the fraction of FUV light, emitted by young stars, that is absorbed by dust is directly proportional to the fraction that is reemitted in the IR (wavelength range 8 – 1000 $\mu$ m), as is often assumed in the literature.

### $2.3. \ \ Constraining \ the \ FUV+IR \ SFR \ distributions$

Under the assumption of a monotonous increasing relation between  $L_X$  (X=FUV or IR) and  $M_*$ , Eqn. (8) shows how this relation, or more generally, the respective luminosity conditional probability distribution, maps the GSMF of SFGs into the FUV or IR LF. These FUV and IR luminosity distributions are tracers of the respective SFR distributions, which combined provide the total SFR conditional probability distribution given  $M_*$  (Eqn. 5). Our final aim is to constrain self-consistently these SFR distributions (FUV, IR, and the total) from observations. Figure 1 summarizes the steps described in the previous subsections and here. The steps are as follows:

Step 1: Define the SFR conditional probability distributions  $\mathcal{P}_{\psi,\mathrm{FUV}}$  and  $\mathcal{P}_{\psi,\mathrm{IR}}^{4}$  as lognormal functions. Propose parametric functions for the mean relations  $\langle \log \mathrm{SFR}_{\mathrm{FUV}}(M_{*}) \rangle$  and  $\langle \log \mathrm{SFR}_{\mathrm{IR}}(M_{*}) \rangle$ , Eqns. (3) and (4), respectively.

Table 1. FUV LFs

Author	Redshift			
Cucciati et al. (2012)	0.05 < z < 4.5			
Arnouts et al. (2005)	0.055 < z < 3.5			
Driver et al. (2012)	0.013 < z < 0.1			
Robotham & Driver (2011)	0.013 < z < 0.1			
Oesch et al. (2010)	$0.75 \lesssim z \lesssim 2.5$			
Alavi et al. (2016)	1 < z < 3			
Hathi et al. (2010)	1 < z < 3			
Mehta et al. (2017)	1.4 < z < 3.6			
Reddy & Steidel (2009)	1.9 < z < 3.4			
Alavi et al. (2014)	$z \sim 2$			
Parsa et al. (2016)	2 < z < 4			
van der Burg et al. (2010)	3 < z < 5			
Ono et al. (2018)	4 < z < 7			
Bouwens et al. (2007)	$4\lesssim z\lesssim 5$			
Finkelstein et al. (2015)	$4 \lesssim z \lesssim 8$			
Bouwens et al. (2015)	$4\lesssim z\lesssim 8$			
Atek et al. (2018)	$z \sim 6$			
Livermore et al. (2017)	6 < z < 8			
Bhatawdekar et al. (2019)	6 < z < 9			
Bouwens et al. (2011)	$7\lesssim z\lesssim 8$			
Oesch et al. (2012)	$z \sim 8$			

- Step 2: Convert SFRs into luminosities using the Kennicutt (1998) conversion factors. This allows us to pass from the conditional distributions  $\mathcal{P}_{\psi,\text{FUV}}$  and  $\mathcal{P}_{\psi,\text{IR}}$  to the conditional distributions  $\mathcal{P}_{l,\text{FUV}}$  and  $\mathcal{P}_{l,\text{IR}}$ , respectively.
- Step 3: Characterize the redshift evolution of the observational GSMF of SFGs,  $\phi_{SF,g}$ . Appendix A presents our best fitting model to the compiled GSMFs and fractions of SFGs as a function of redshift from Rodríguez-Puebla et al. (2017).
- **Step 4:** Derive the FUV and IR LFs by convolving the GSMF of SFGs with their corresponding conditional luminosity distributions (Eqn. 8):  $\phi_{\text{FUV}} = \mathcal{P}_{l,\text{FUV}} \circledast \phi_{\text{SF},g}$  and  $\phi_{\text{IR}} = \mathcal{P}_{l,\text{IR}} \circledast \phi_{\text{SF},g}$ .
- Step 5: Constrain the redshift-dependent parameters of the mean  $\langle \log \mathrm{SFR_{FUV}}(M_*) \rangle$  and  $\langle \log \mathrm{SFR_{IR}}(M_*) \rangle$  relations. This is possible since steps 1-4 relate the mean relations to the observed FUV and IR LFs.

Once the redshift-dependent parameters of the mean  $\langle \log SFR_{FUV}(M_*) \rangle$  and  $\langle \log SFR_{IR}(M_*) \rangle$  relations are constrained the total conditional SFR distribution for

 $<sup>^3</sup>$  Using the conversion factors is a very popular approach to empirically relate SFRs to luminosities. While there is some justification in using this method, it provides, nevertheless, with values that could differ from the real ones. For example, the conversion factor of the SFR diagnostic based on the FUV light depends on the metal-enrichment and the star formation history, SFH, of a galaxy. This could lead to difference up to  $\sim 0.5$  dex in the conversion factor when exploring different combinations of these dependencies (see figure 3 from Madau & Dickinson 2014, see also Tacchella et al. 2018). While the above introduces an uncertainty that could be taken into account in our analysis, we decided to use the most popular calibration factors from the literature because this facilitates the comparison with previous works. Therefore, we do not consider more complex conversion factors that depend on metallicity and SFHs.

<sup>&</sup>lt;sup>4</sup> Note that we use here  $\mathcal{P}_{\psi,\mathrm{IR}}$  and not  $\mathcal{P}_{\psi,\mathrm{IR-SF}}$  since the IR LFs to be used are for all SFGs, including starbursts. Posteriorly, we can separate  $\mathcal{P}_{\psi,\mathrm{IR}}$  into  $\mathcal{P}_{\psi,\mathrm{IR-SF}}$  and  $\mathcal{P}_{\psi,\mathrm{IR-SB}}$ .

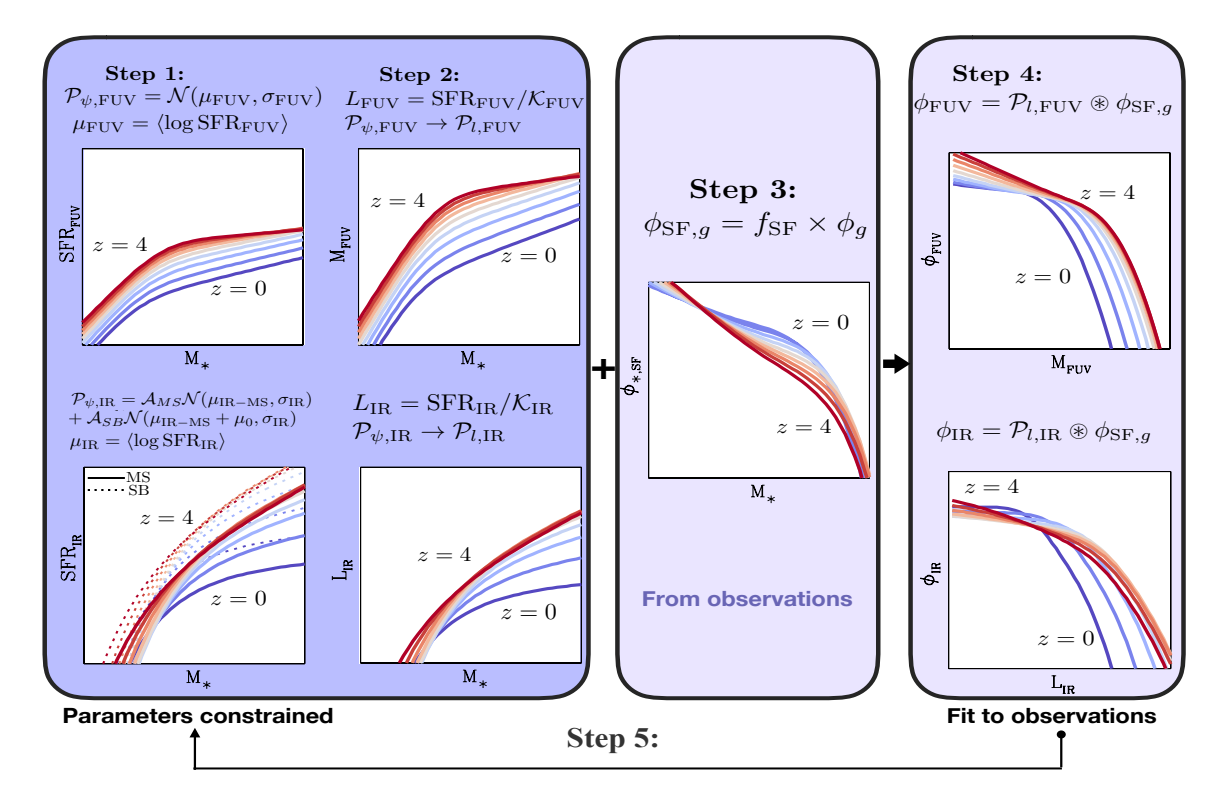


Figure 1. Scheme with the steps to constrain the means of SFR given  $M_*$  at different redhsifts from fitting the observational FUV and IR LFs and knowing the GSMFs of SFGs; see text for details.

MS galaxies is given by Eqn. (5) while the mean  $\langle \log \mathrm{SFR}(M_*) \rangle$  relation and scatter are given by Eqs. (6) and (7), respectively. Next, we describe the parametrization and the best fitting model to the redshift evolution of the mean  $\mathrm{SFR}_{\mathrm{FUV}}-M_*$  and  $\mathrm{SFR}_{\mathrm{IR}}-M_*$  relations.

Each of the parameters described by Equations (3) and (4) depend on redshift. After some experimentation, we found that the redshift dependence of these parameters is well described by the following function:

$$Q(q_1, q_2, q_3, z) = q_1 + q_2 \log(1+z) + q_3 z^2.$$
 (10)

In this paper, we find the best fitting parameters by using a Bayesian approach through a MCMC method applied jointly to the data following Rodríguez-Puebla et al. (2013).

Figure 2 shows a compilation of measured rest-frame FUV LFs between z=0 and z=9.5 from 21 observational studies that are listed in Table 1. The FUV LFs were not corrected for dust attenuation but homogenized to our adopted cosmology. We use this compilation to find the best fit parameters to the evolution of the mean  $SFR_{FUV}-M_*$  relationship. The solid lines in Figure 2 show our best fitting model to the LF  $\phi_{\rm obs,FUV}$ . The best fit parameters of the redshfit-dependent mean

 $SFR_{FUV}-M_*$  relationship are:

$$\mu_{\text{FUV},0}(z) = \mathcal{Q}(-1.451 \pm 0.011, -2.471 \pm 0.027, \\ -0.001 \pm 4 \times 10^{-4}, z),$$
(11)

$$\log M_{\text{FUV}}(z) = \mathcal{Q}(8.343 \pm 0.011, -0.705 \pm 0.030, 0.002 \pm 7 \times 10^{-4}, z),$$
(12)

$$\alpha(z) = \mathcal{Q}(-0.543 \pm 0.009, -1.978e - 0.05 \pm 0.002, 0.010 \pm 2 \times 10^{-4}, z),$$
(13)

$$\beta(z) = \mathcal{Q}(0.667 \pm 0.006, -0.033 \pm 0.015, 0.012 \pm 4 \times 10^{-4}, z).$$
(14)

The observational IR LFs from z=0 to z=4.2 are shown in Figure 3 from a compilation of 8 observational studies listed in Table 2. Similarly above the data was homogenized to our adopted cosmology. Using these data, as in the case of the FUV data, we constrain the best fit parameters of the redshift-dependent mean  $SFR_{IR}-M_*$  relationship:

$$\mu_{\text{IR},0}(z) = \mathcal{Q}(0.127 \pm 0.017, -5 \pm 0.044, \\
-0.168 \pm 0.028, z),$$
(15)

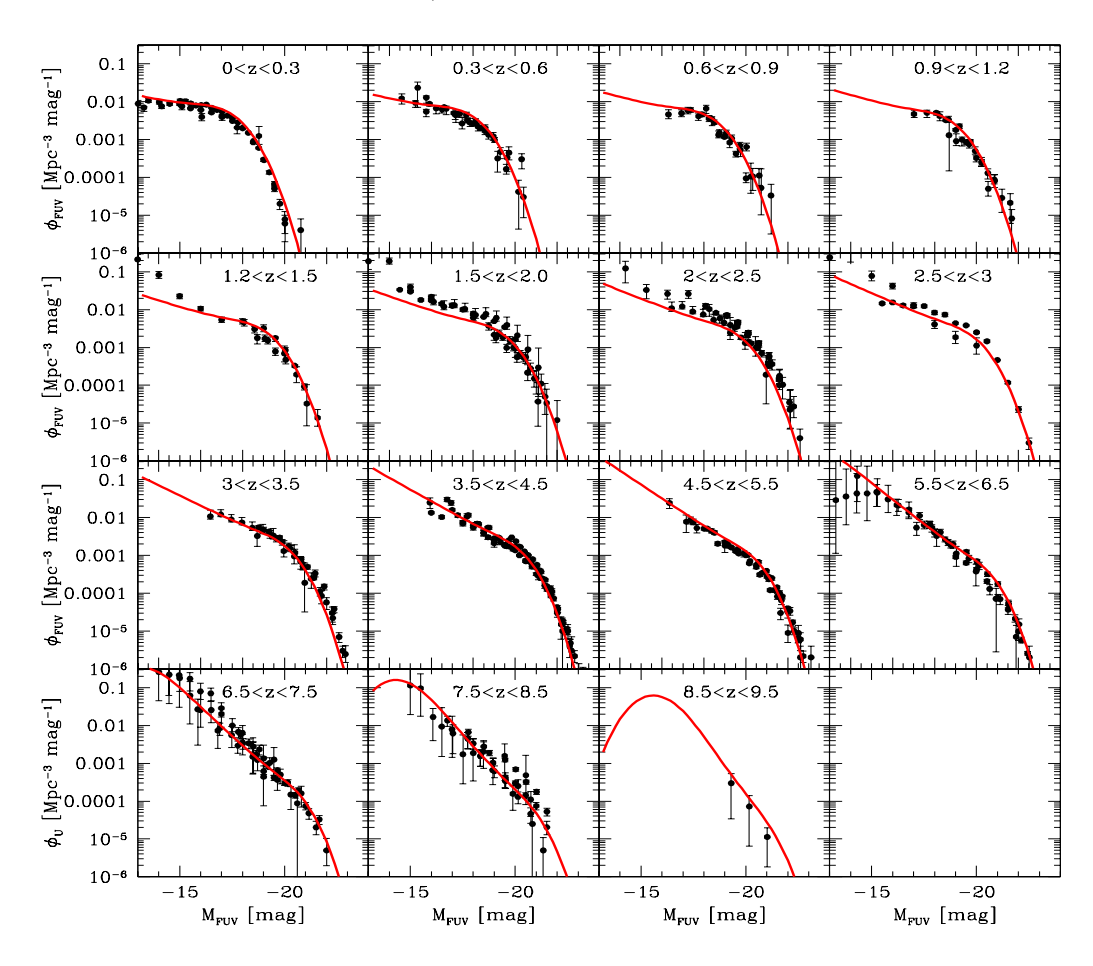


Figure 2. FUV Luminosity Function. The red solid lines present the best fitting models to a compilation of 21 observational studies, see Table 1. The data has been homogenized to a same cosmology. The turn over at the faint end at z > 7.5 is due to the lower limit of  $M_*$  considered for the integral in Equation (8).

$$\log M_{\rm IR}(z) = \mathcal{Q}(9.850 \pm 0.031, -1.876 \pm 0.087, -0.107 \pm 0.030, z),$$
(16)

$$\gamma(z) = \mathcal{Q}(0.051 \pm 0.011, 0.983 \pm 0.066, 0, z). \tag{17}$$

Our best fitting model is shown with the red solid lines in Figure 3.

#### 3. RESULTS

Before discussing our results, we note that the IR LF is the main source of uncertainty in all the conclusion that will be presented below. This is due to its restricted redshift,  $z\lesssim 4$ , and luminosity range, see Figure 3. This is not the case for the FUV LF and the GSMF which are available up to  $z\sim 9$  and cover several orders of magnitude from low- to high-luminosity/mass galaxies, see Figures 2 and also Figure 11 from Appendix A. In order to reduce the risk of over-interpreting our results, in the

Table 2. IR LFs

Author	Redshift		
Eser et al. (2017)	0 < z < 0.3		
Le Floc'h et al. (2005)	0 < z < 1		
Casey et al. (2012)	0 < z < 1.6		
Lim et al. (2020)	0 < z < 4		
Gruppioni et al. (2013)	0 < z < 4.2		
Magnelli et al. (2013)	0.1 < z < 2.3		
Magnelli et al. (2011)	1.3 < z < 2.3		

figures below we will indicate explicitly the regimes over which our IR LFs are valid.  $^5$ 

In Figure 4 we present our resulting  $\langle \log SFR \rangle$  as a function of redshift for five stellar mass bins. The solid

 $<sup>^{5}</sup>$  The exception will be Figure 9, but this is discussed in the text.

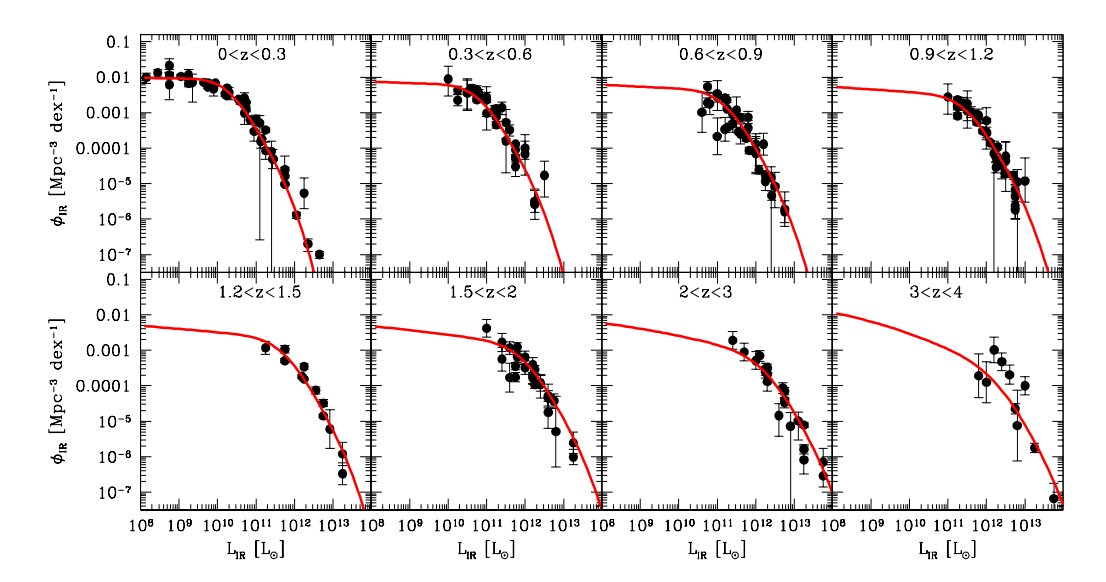


**Figure 3.** IR Luminosity Function. Solid lines present the best fit from a compilation of 7 observational studies, see Table 2. Similarly to the FUV LFs, the data has been homogenized to a same cosmology

lines indicate the stellar mass ranges when the best fitting models of both the FUV and IR LFs are constrained by the data. The dashed lines indicate the range over which the IR LFs have been extrapolated but there are observational data to constrain the best fit models of the FUV LF. The shaded area shows the scatter around the mean relation using Equation (7). Note that the above limitation in the data affects mostly low-mass galaxies,  $M_* \lesssim 10^9 {\rm M}_{\odot}$ .

Figure 4 compares our results to several observational studies listed in Table 3 for galaxies with masses above  $M_* \sim 0.5 - 1 \times 10^9 {\rm M}_{\odot}$ . The compiled data has been homogenized to a same Chabrier (2003) IMF. In addition, in the cases that the authors report the mean  $\langle SFR \rangle$  we use Equation (2) to transform into the mean  $\langle \log SFR \rangle$ . We also compute the mean SFR- $M_*$  relationship at  $z \sim 0$  for SDSS galaxies using the GALEX-SDSS-WISE Legacy catalogue (GSWLC, Salim et al. 2016, 2018). Here we use their deep GSWLC-2 catalogue which uses UV, optical and  $22\mu m$  from WISE to derive SFRs from SED fitting techniques, for details see Salim et al. (2018). From this catalog, we use their SFRs derived using both the UV and IR components and we define MS SFGs following Fang et al. (2018). In Figure 4 the colors indicate the different calibrators reported by the authors. Note, however, that most of the data compiled in this paper are based on FUV+IR measurements, for a more direct comparison to our results.

In excellent agreement with the set of independent observations from Table 3, our results reproduce both the strong evolution of the SFR with z and the dependence

on  $M_*$ . The above is also true when using the extrapolation from the IR LF.

Figure 5 shows the obtained sSFR- $M_*$  relation for MS galaxies from  $z \sim 0$  to  $z \sim 4$ . Here, our results are also in excellent agreement with the compiled data. This is actually not trivial since the compilation described above is composed of measurements based on different surveys and calibrators (though mostly are based on FUV+IR measurements). We thus conclude that our derived SFRs describe quite well a set of independent observational inferences over the range where both the IR and FUV LFs are available. A straightforward implication from the above is that the joint evolution of the GMSF and the FUV and IR LFs is self-consistent, that is, the evolution of the FUV+IR SFR of MS galaxies is consistent with their stellar mass growth. The reason for this is that in our approach the FUV+IR LF is the result of convolving the GSMF of SFGs with the SFR conditional distribution given  $M_*$ , see Equation (9) and Figure 1.

We notice that our derived sSFR- $M_*$  relations at all redshifts are not well described by simple power laws. A curvature in the MS has been already documented in previous works (see e.g., Lee et al. 2015; Tomczak et al. 2016; Popesso et al. 2019b). In general, our MS at any z follows a power law only at the high-mass end, with the mass at which the relation departs from the power law decreasing with z, roughly, from  $M_* \sim 10^{11}$  at z > 2 to  $M_* \sim 2 \times 10^{10}$  at  $\sim 0$ . At lower masses and at any redshift, the MS bends until an inflection point is attained. In the sSFR- $M_*$  plane, this means that the MS changes of sign. This is an interesting feature of

Table 3. Star Formation Rates

Author	SFR indicator	$\Delta_{ m SFR}[ m dex]$	$\Delta_{\mathrm{M}_{*}}[\mathrm{dex}]$	$\sigma_{ m SFR}[{ m dex}]$	Redshift
Popesso et al. (2019a,b)	UV+IR	0	0	0.25 - 0.4	0 < z < 2.5
Lee et al. (2015)	UV+IR	-0.15	0	0.36	0.2 < z < 1.3
Ilbert et al. (2015)	UV+IR	0	0	0.22 - 0.48	0.2 < z < 1.4
Whitaker et al. (2012)	UV+IR	-0.15	-0.03	0.34	0.5 < z < 2.5
Whitaker et al. (2014)	UV+IR	-0.13	0	$0.34^{a,b}$	0.5 < z < 2.5
Tomczak et al. (2016)	UV+IR	-0.13	0	$0.34^{a,b}$	0.5 < z < 4
Schreiber et al. (2015)	UV+IR	-0.31	-0.2	0.31	z < 4
Reddy et al. (2012)	UV+IR & SED	-0.2	-0.2	0.37	1.4 < z < 3.7
Salmon et al. (2015)	UV	-0.2	-0.2	0.25 - 0.41	$z \sim 4$
González et al. (2011)	UV	-0.2	-0.2	$0^a$	$z \sim 4$
Bouwens et al. (2012)	UV	-0.2	-0.2	$0.3^{a,c}$	$z \sim 4$
Duncan et al. (2014)	UV	0	0	0.28	$z \sim 4$
Karim et al. (2011)	$1.4~\mathrm{GHz}$	$+0.18^{d}$	-0.02	$0^a$	0.2 < z < 0.4
Karim et al. (2011)	$1.4~\mathrm{GHz}$	$+0.15^{d}$	-0.02	$0^a$	0.4 < z < 0.6
Karim et al. (2011)	$1.4~\mathrm{GHz}$	$+0.11^{d}$	-0.02	$0^a$	0.6 < z < 0.8
Karim et al. (2011)	$1.4~\mathrm{GHz}$	$+0.07^{d}$	-0.02	$0^a$	0.8 < z < 1
Karim et al. (2011)	$1.4~\mathrm{GHz}$	$+0.03^{d}$	-0.02	$0^a$	1 < z < 1.2
Karim et al. (2011)	$1.4~\mathrm{GHz}$	$-0.01^{d}$	-0.02	$0^a$	1.2 < z < 1.6
Karim et al. (2011)	$1.4~\mathrm{GHz}$	$-0.07^{d}$	-0.02	$0^a$	1.6 < z < 2.0
Karim et al. (2011)	$1.4~\mathrm{GHz}$	$-0.12^{d}$	-0.02	$0^a$	2.0 < z < 2.5

NOTE— $\Delta_{SFR}$  and  $\Delta_{M_*}$  are the correction offsets. Correction to a same IMF and when authors report  $\langle SFR \rangle$  instead of  $\langle \log SFR \rangle$  were applied.

the MS at low masses that our method allowed us to establish. Following, we discuss it in more detail.

# 3.1. The Main Sequence of low-mass and dwarf galaxies

Here, we explore our results for low-mass galaxies  $10^8 \lesssim M_*/{\rm M}_\odot \lesssim 10^9$ . Our low-mass limits are restricted by the observational availability of both the FUV and IR LFs. This affects the robustness of our derivations at masses below  $M_* \sim 5 \times 10^9 {\rm M}_\odot$ , in particular for redshifts larger than  $z \sim 0.5$ . For low mass galaxies, our results are based mainly on the FUV LFs, and to a lesser extent to the extrapolations of the IR LFs, due to the flat faint-end slopes of the latter (see Figure 3). Therefore, it is important to understand the robustness of our inferences for low-mass galaxies and the impact of our extrapolations from the IR LFs.

We begin by noticing that previous authors reported a strong dependence of dust-obscured star formation with stellar mass as follows: the SFRs of galaxies with  $M_* \gtrsim 10^9 {\rm M}_{\odot}$  are mainly traced by the IR light while the FUV light is more important for lower mass galaxies, and this trend is consistent with no redshift dependence (e.g., Pannella et al. 2009; Whitaker et al. 2017). If we extrapolate the above results to our derivations then the implication is straightforward: for low-mass galaxies  $M_* \lesssim 10^9 {\rm M}_{\odot}$ , the FUV LF is more important for the total SFR than the IR LF. In other words, little or no dust corrections are required for the FUV-based SFRs of low-mass galaxies. In consequence, our resulting trends with mass and redshift for low-mass galaxies, that are dominated by FUV, will be in the right direction. The above is also supported by Figures 8 and 9 that we will discuss below. In the light of the above, next we describe our results for low-mass galaxies.

Figure 5 shows evidence that the sSFR- $M_*$  relation for MS galaxies *bends*, and even the slope sign changes, at the low-mass end at all redshifts. Why does the sSFR- $M_*$  relation change of sign at the low-mass end?

<sup>&</sup>lt;sup>a</sup> No measure of the scatter available.

<sup>&</sup>lt;sup>b</sup> We assumed  $\sigma_{\rm SFR} = 0.34$  as in Whitaker et al. (2012).

<sup>&</sup>lt;sup>c</sup> We assumed  $\sigma_{\rm SFR}=0.3$ .

<sup>&</sup>lt;sup>d</sup> Corrections taken from Speagle et al. (2014)

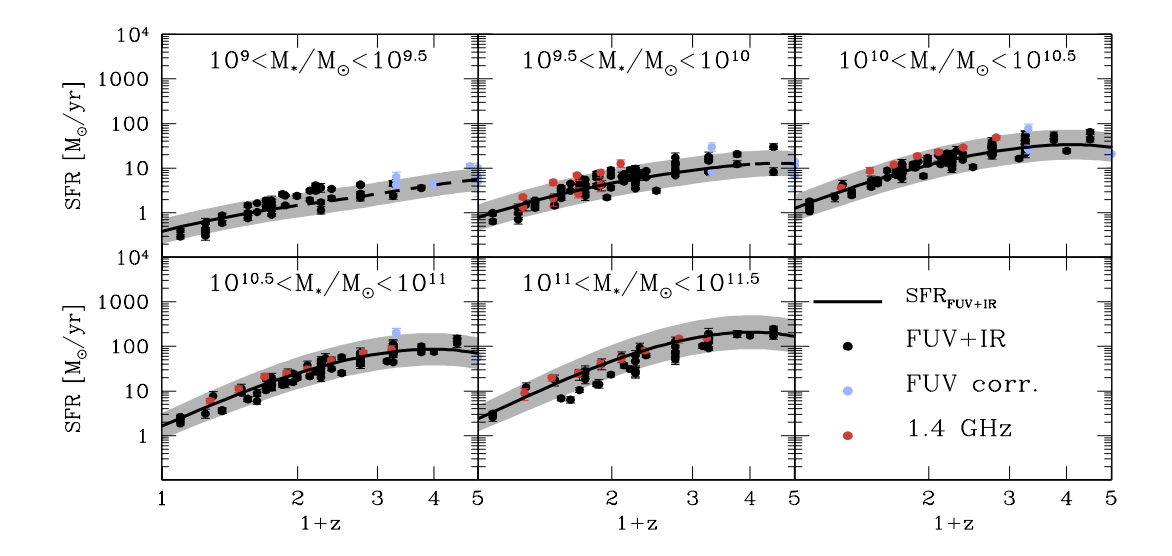
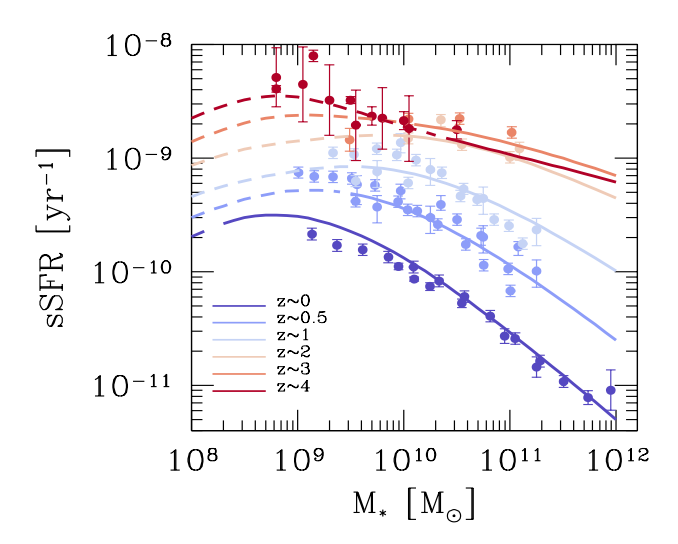


Figure 4. SFRs as a function of redshift for five stellar mass bins. The solid lines show our results when the best fitting models of both the FUV and IR LFs are available. The dashed lines show the mass regimes when the IR LFs have been extrapolated but the FUV LFs are available. The filled circles with error bars show the compilation reported from Table 3 for SFGs from galaxy surveys. Black circles show the results based on FUV+IR, while light blue and red circles show the results based on FUV dust-corrected and radio data. Note that our results are in good agreement with the inferences from galaxy surveys.



**Figure 5.** The sSFR- $M_*$  relation for MS SFGs from  $z\sim 0$  to  $z\sim 4$ . The solid lines show our results when the best fitting models of both the FUV and IR LFs are available. The dashed lines show the mass regimes when the IR LFs have been extrapolated but the FUV LFs are available. The filled circles with error bars show the compilation from Table 3 for MS SFGs. Our results are consistent with the inferences from galaxy surveys.

To answer this, recall that the SFRs from low mass galaxies,  $M_* \lesssim 10^9 {\rm M}_{\odot}$ , are dominated by the FUV component. The upper and bottom panels of Figure

6 show the corresponding  $M_{FUV}-M_*$  and  $sSFR_{FUV}-M_*$ relationships. An important trend is apparent here. The  $\rm sSFR_{FUV}-M_*$  relation bends below  $M_* \sim 10^9 \rm M_{\odot}$ , similarly to the sSFR- $M_*$  relation. Not surprising, this bend is inherited by the turnover of the  $M_{FUV}-M_*$  relation. The next important feature to notice is that the turnover mass of the  $M_{FUV}-M_*$  relation is nearly constant with redshift,  $\sim 5 \times 10^8 \mathrm{M}_{\odot}$ , but  $\mathrm{M}_{\mathrm{FUV}}$  changes from  $M_{\rm FUV} \sim -16$  at  $z \sim 0$  to  $M_{\rm FUV} \sim -20$  at  $z \sim 4$ . By looking to Figure 2, it is then evident that the above magnitudes correspond to the knee of the FUV LF. It is now clear that the bending in the sSFR- $M_*$  is due the knee of the FUV LF. In general, it is important to note that the form of the  $M_{FUV}-M_*$  and  $sSFR_{FUV}-M_*$  relations are governed by the Schechter-like shapes of the FUV LF. Individual determinations for low mass galaxies at high redshifts will be key to confirm the above and for studying the self-consistency of the joint evolution of the faint end of the GSMF and the FUV+IR LFs. Fortunately, more accurate observational constraints are available at low masses for nearby galaxies, so, we now focus our discussion to low-mass and dwarf galaxies at  $z \sim 0$ .

Figure 7 presents again the sSFR– $M_*$  relationship but this time at  $z\sim 0$  and extending down to dwarf galaxies,  $M_*\sim 7\times 10^7{\rm M}_\odot$ . As noted above, the slope of this relation flattens at low masses and changes sign around  $M_*\sim 5\times 10^8{\rm M}_\odot$ . Additionally, we present separately the contribution from FUV, blue solid line, and IR, red

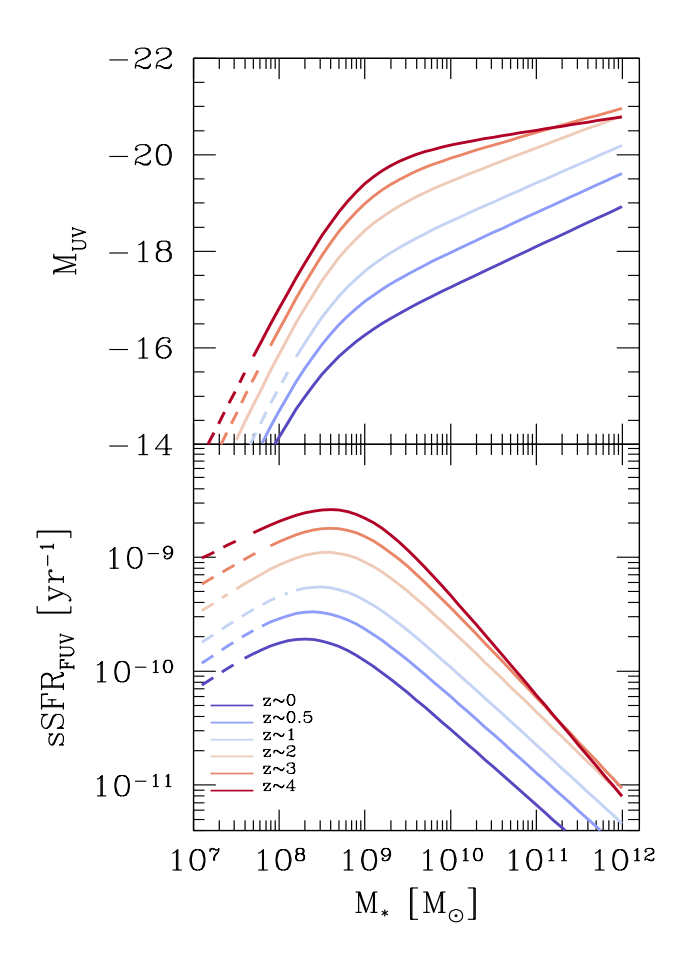


Figure 6. Upper Panel: The  $M_{FUV}-M_*$  relation for MS SFG from  $z\sim 0$  to  $z\sim 4$ . The solid lines show our results constrained by our best fitting models of the FUV LF. The dashed lines show the mass regimes when the FUV LFs have been extrapolated. Bottom Panel: The sSFR<sub>FUV</sub>- $M_*$  relation for MS SFGs from  $z\sim 0$  to  $z\sim 4$ . Notice the bend in the sSFR<sub>FUV</sub>- $M_*$  relationship corresponds to the knee of the FUV LF, Figure 2.

solid line, SFRs. Notice that the mass around which the slope of the sSFR– $M_*$  relationship changes of sign is close to the mass above which the regime of dust-obscured star formation starts to dominate,  $M_* \sim 6 \times 10^8 {\rm M}_{\odot}$ .

Similarly to Figure 5, we compare our results with our compilation at  $z\sim 0$ , gray stars with error bars. At low masses, we add our estimates of the (total) sS-FRs to the KINGFISH sample from Skibba et al. (2011) obtained with GALEX and the Herschel Space Observatory data, filled black circles. We also compute the average sSFR from a sample of low-mass galaxies at the mass range  $10^{8.5} \lesssim M_*/\rm M_{\odot} \lesssim 10^9$  with an axis ratio of  $b/a \geq 0.5$  from the MaNGA/SDSS-IV survey (Cano-

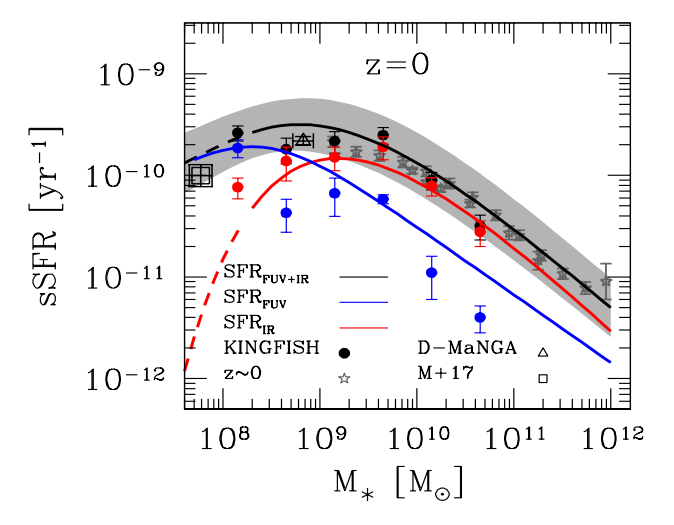


Figure 7. The sSFR- $M_*$  relation for MS SFGs at  $z\sim 0$  over a broad mass range:  $M_*\sim 7\times 10^7-10^{12}{\rm M}_\odot$ , black solid line. The contributions from FUV and IR are shown separately with blue and red solid lines respectively. The gray stars with error bars correspond to the compilation from Table 3. The solid black circles corresponds to the total SFRs based on the KINGFISH sample from Skibba et al. (2011), while the blue and red solid circles correspond to the contributions from FUV and IR respectively. The open triangle shows the average sSFR from a sample of low-mass galaxies at the mass range  $10^{8.5} \lesssim M_*/{\rm M}_\odot \lesssim 10^9$  from the MaNGA/SDSS-IV survey (Cano-Diaz in prep.). The open square shows the results from a sample of dwarf galaxies from McGaugh et al. (2017) at  $10^{7.5} \lesssim M_*/{\rm M}_\odot \lesssim 10^8$ . Our results are consistent with this set of independent observations for local galaxies.

Diaz in prep.).<sup>6</sup> Finally, from a sample of dwarf galaxies from McGaugh et al. (2017) we compute the average sSFR at the mass range  $10^{7.5} \lesssim M_*/{\rm M}_{\odot} \lesssim 10^8$ , open square. Notice that both for the MaNGA and the McGaugh et al. (2017) samples SFRs were derived from  ${\rm H}_{\alpha}$  luminosities. We transform their  ${\rm H}_{\alpha}$  determinations into dust-corrected SFR<sub>FUV</sub> by using eq. 16 from Shin et al. (2019). In general, our results for the total SFRs are in good agreement with the above observations down to  $M_* \sim 7 \times 10^7 {\rm M}_{\odot}$ .

In the case of the KINGFISH sample, the authors reported IR luminosities (see their table 1) which we transform into SFRs (red circles). We also subtract IR SFRs

<sup>&</sup>lt;sup>6</sup> The methodology to derive the SFRs and to select the SF galaxies are both explained in detail in Cano-Díaz et al. (2019). In this work we use the data products provided by the Pipe3D Value Added Catalogue (Sánchez et al. 2018), which uses the Integral Field Spectroscopy analysis pipeline, Pipe3D (Sánchez et al. 2016), for the last MaNGA public data release: version v2-4-3.

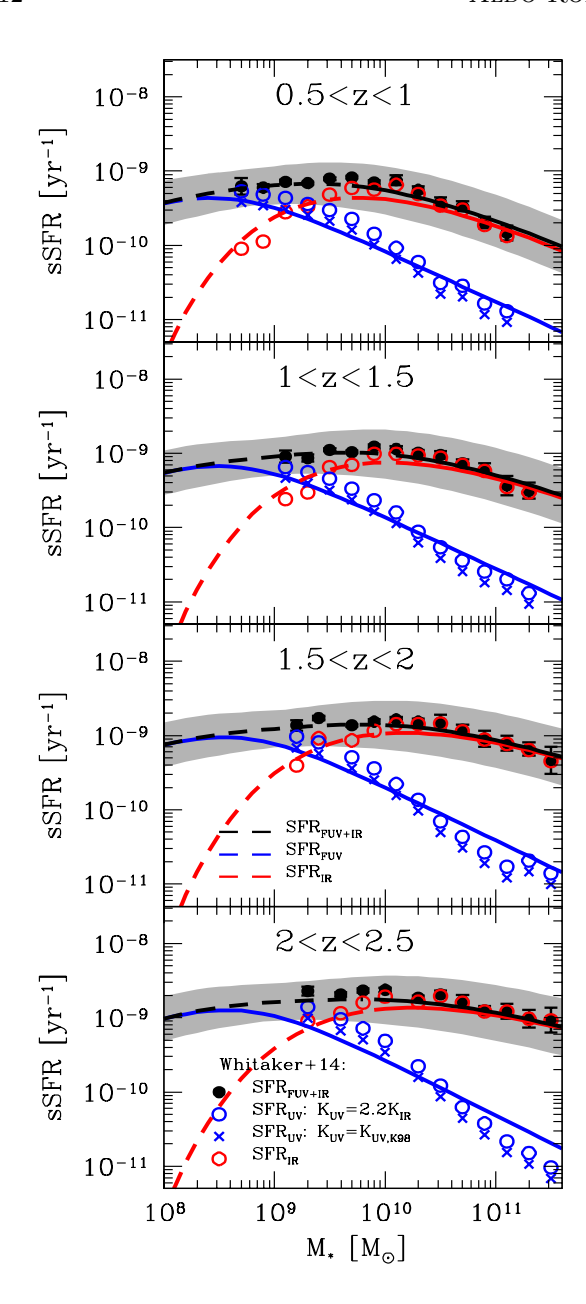


Figure 8. The predicted total average sSFR- $M_{\ast}$  relation and the contribution from FUV and IR light from z=0.5 to z=2.5. We compare to the inferences from Whitaker et al. (2014). Similarly to Figure 5, the solid lines show our resulting sSFRs where both the best fitting models from the FUV and IR LFs are valid while the dashed lines show where the FUV LF is valid but the IR LF has been extrapolated. Our results are consistent with the total SFRs from Whitaker et al. (2014) as well as for the FUV and IR contributions, even in the regimes where we have extrapolated our results.

from the total in order to compute UV SFRs (blue circles) according to their eq. 7. It is encouraging that our results reproduce pretty well the observational trends from the KINGFISH sample. Remarkably, both our results and the KINGFISH sample appear to have a similar characteristic mass,  $M_{*,\rm obsc} \sim 6 \times 10^8 {\rm M}_{\odot}$ , above which the SFRs are dust-obscured. We thus confirm that the FUV light becomes more important as a diagnostic of the SFR of dwarf galaxies.

## 3.2. The redshift evolution of the FUV and IR contribution to the total SFR

In Figure 8, we explore the contribution of FUV and IR to the total sSFR– $M_*$  relationship at  $0.5 \le z \le 2.5$ . Similarly to Figure 5, the solid lines show the mass regime where the best fitting models of both the FUV and IR LFs are constrained by the data while the dashed lines show the stellar mass regime where the LFs were extrapolated.

We compare our results with the total SFRs reported from Whitaker et al. (2014) computed as the combination of the UV<sup>7</sup> and IR values based on the Spitzer/ MIPS 24  $\mu$ m photometry. Note that we subtract  $\sim 0.13$ dex to their SFRs in order to convert from log(sSFR) to  $\langle \log sSFR \rangle$ , see Equation (2) and Table 3. In the same figure we present separately the contribution from FUV and IR by using the average luminosities,  $\langle L \rangle (M_*)$ , reported in their table 2. Note that we plotted two different symbols for the SFR<sub>FUV</sub> from Whitaker et al. (2014). The open circles show the conversion factor utilized by Whitaker et al. (2014) of  $\mathcal{K}_{FUV} = 2.2 \times \mathcal{K}_{IR} =$  $2.4 \times 10^{-10} \rm M_{\odot} \ yr^{-1} \it L_{\odot}^{-1}$  while the cross symbols use the conversion factor utilized in this paper, see Section 2. The conversion factors used by Whitaker et al. (2014) results in a factor of  $\sim 1.4$  larger than ours. Thus, the cross symbols are more adequate for comparing with our results.

In general, when comparing to Whitaker et al. (2014) we observe that our results capture the same trends to the contributions from FUV and IR at all masses and redshifts, even for the regimes where we extrapolated our results from the IR LFs, red dashed-lines. Note that the FUV component dominates the low-mass regime both in our and in the Whitaker et al. (2014) results. This is encouraging and hints again that the trends reported in Figures 5 and 7 for the total SFRs at the low-mass regime are in the right direction.

 $<sup>^7</sup>$  Whitaker et al. (2014) estimated UV luminosities as the integrated light within the range between 1260–3000 Å by using the 2800 Å rest-frame luminosity:  $L_{\rm UV}(1260-3000 {\rm \AA})=1.5 \nu L_{\nu,2800}.$ 

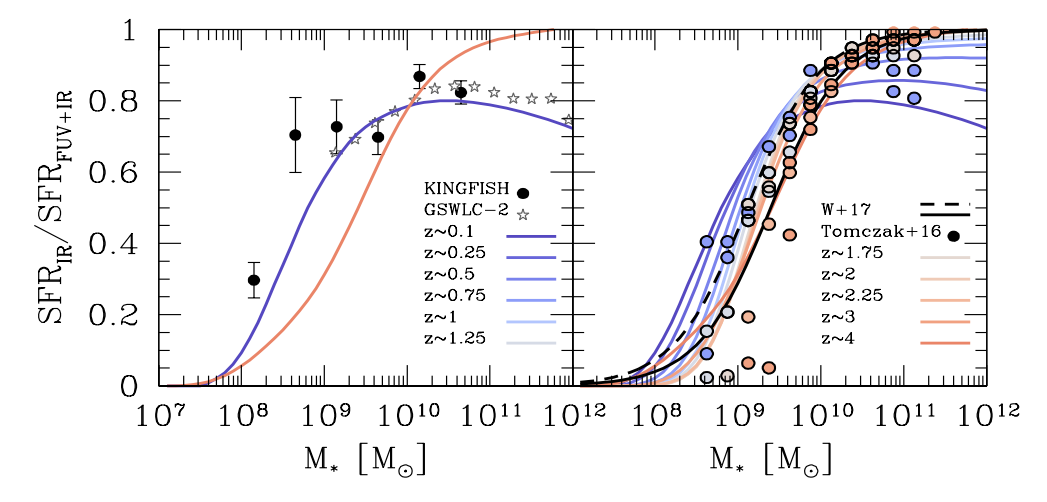


Figure 9. Redshift evolution for the fraction of obscured star formation. Left panel: The violet solid line show our results at  $z \sim 0.1$  while the filled black circles show the determinations from Skibba et al. (2011) based on the KINGFISH sample The gray stars show the determinations of using the dust attenuation values  $A_{\rm FUV}$  reported in the GSWLC-2 (Salim et al. 2018). For comparison we show the results at  $z \sim 4$ . The fraction of obscured star formation evolves with redshift. Right panel: The solid lines show the results based on our approach from  $z \sim 0.1$  to  $z \sim 4$  while the filled circles show the results from Tomczak et al. (2016) based on their reported luminosities  $\langle L_{\rm FUV} \rangle$  and  $\langle L_{\rm IR} \rangle$ . The black solid line is the best fit to observations from Whitaker et al. (2017) using the FUV estimator from Whitaker et al. (2014) while the dashed line show the results based on the Murphy et al. (2011) FUV estimator.

Regarding the characteristic mass for the transition to the dust-obscured star formation regime,  $M_{*,\rm obsc}$ , we observe an evolution from  $z\sim 0$  to  $z\sim 2.5$  of  $\sim 3.3$ , the values are respectively  $M_{*,\rm obsc}\sim 6\times 10^8{\rm M}_{\odot}$  and  $M_{*,\rm obsc}\sim 2\times 10^9{\rm M}_{\odot}$ . From  $z\sim 0.5$  to  $z\sim 2.5$  the characteristic mass has evolved a factor of  $\sim 2.2$ . A similar trend is observed based on the results from Whitaker et al. (2014) and reported explicitly in Whitaker et al. (2017).

# 3.3. Mass and redshift dependence of the obscured star formation regime

According to Figures 7 and 8, our results are consistent with the observational samples that separate the contributions from FUV and IR from  $z\sim0$  to  $z\sim2.5$ , even when we extrapolated our results for the IR LFs. In the following we will use our results based on the extrapolations of the IR LFs as direct predictions from our approach.

The left panel of Figure 9 presents our resulting fraction of dust-obscured star formation as a function of stellar mass at  $z\sim 0$ , violet solid line. Figure 9 shows that our results have a strong dependence with stellar mass in the direction that the SFRs of high-mass galaxies are more obscured by dust than low-mass galaxies at  $M_*\sim 10^{10} \rm M_{\odot}$  the dust-obscured fraction approaches to a maximum value of  $\sim 0.8$  and for larger masses it keeps roughly constant. The filled circles show the results from the KINGFISH sample. The gray stars show the results of using the dust attenuation values  $A_{\rm FUV}$  re-

ported in the GSWLC-2 catalog. Both, the KINGFISH sample and GSWLC-2 catalog are in good agreement with our results. For comparison, we plot our dust-obscured fraction at  $z\sim 4$ , light red solid line. Notice that the results at  $z\sim 4$  are inconsistent with the local determinations indicating the obscured fraction evolves with redshift. Next, we discuss the comparison with high redshift data.

The right panel of Figure 9 presents the fraction of dust-obscured star formation as a function of stellar mass from  $z \sim 0$  to  $z \sim 4$ . The fraction of the dustobscured SFRs evolves mostly from  $z \sim 0$  to  $z \sim 1.2$ but above  $z \sim 1.2$  our results are consistent with little evolution up to  $z \sim 4$ . We reproduce the best fitting model to the fraction of dust-obscured SFRs from Whitaker et al. (2017) at  $0.5 \le z \le 2.5$  using their "standard calibration", black solid line, and their best fitting model based on the Murphy et al. (2011) calibration parameters, dashed lines. We note a remarkable agreement between our results with those from Whitaker et al. (2017) when considering both of their calibrators. We also compute the fraction of dust-obscured SFRs using the luminosities  $\langle L_{\rm FUV} \rangle$  and  $\langle L_{\rm IR} \rangle$  reported in table 1 from Tomczak et al. (2016), filled circles. We find again excellent agreement with these authors.

An important feature is worth to mention here. According to our results, at low redshifts,  $z \lesssim 0.75$ , high-mass galaxies have become more "transparent" to UV light compared to their high redshift counterparts. For

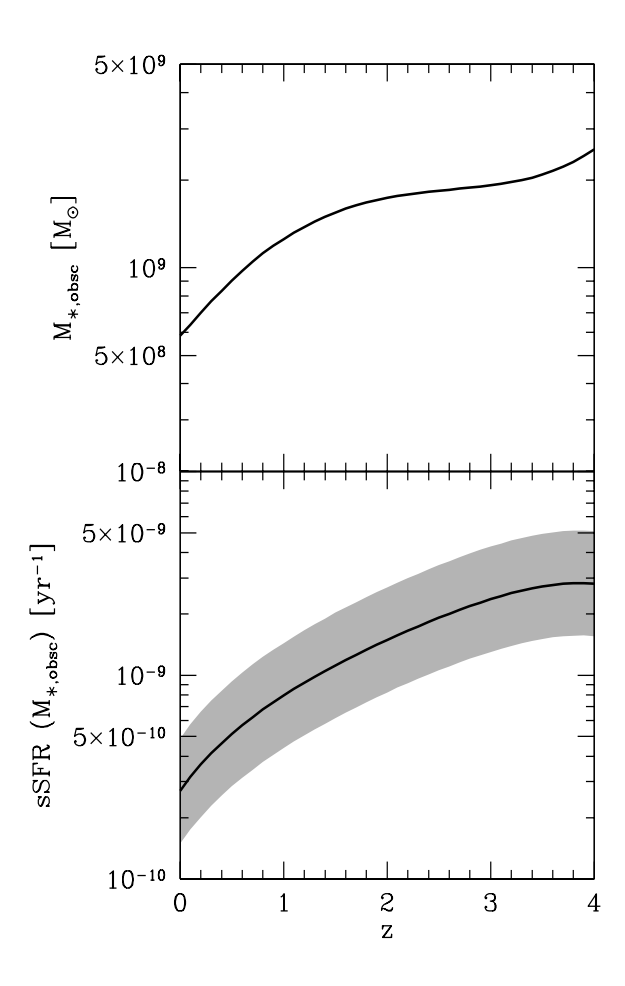


Figure 10. Upper panel: Redshift evolution of the characteristic mass  $M_{*,\mathrm{obsc}}$  that marks the transition between the unobscured and obscured star formation regimes. Notice that since  $z\sim1.5$  the characteristic mass  $M_{*,\mathrm{obsc}}$  decreased by a factor of  $\sim4$  while above  $z\sim1.5$  has increased only slowly. Bottom panel: Corresponding total sSFR of the characteristic mass  $M_{*,\mathrm{obsc}}$ . The sSFRs has decreased an order of magnitude since  $z\sim4$ .

low- and intermediate-mass galaxies we observe the opposite, they have become more obscured by dust. Similar trends are derived when using the Tomczak et al. (2016) dust-obscured fractions.

The top panel of Figure 10 presents the evolution of the characteristic mass,  $M_{*,\mathrm{obsc}}$ , at which the fraction of dust-obscured star formation is 0.5. Here is evident the rapid evolution of  $M_{*,\mathrm{obsc}}$  for,  $z \lesssim 1.2$ , but then it rises only slowly at high redshifts up to a mass of  $M_{*,\mathrm{obsc}} \sim 2 \times 10^9 \mathrm{M}_{\odot}$ , as noted previously. The bottom panel shows the corresponding sSFR of  $M_{*,\mathrm{obsc}}$ . The sSFR( $M_{*,\mathrm{obsc}}$ ) has a strong correlation with z an appears to reach a maximum of sSFR  $\sim 3 \times 10^{-9}$  yr<sup>-1</sup> just before  $z \sim 4$ . The sSFR( $M_{*,\mathrm{obsc}}$ )-redshift relation has decreased an order of magnitude since  $z \sim 4$ .

### 4. SUMMARY AND DISCUSSION

In this paper we present an statistical method for deriving the evolution of the mean sSFR- $M_*$  relation of MS galaxies by combining the FUV and IR rest-frame LFs with the GSMF of SFGs from  $z \sim 0$  to  $z \sim 4$ . The total SFR is estimated as the sum of the unobscured and obscured regimes traced by the FUV (1500Å) and IR  $(8-1000\mu m)$  luminosities, respectively. Our approach is an alternative to the commonly employed procedure in the literature, consisting in using large galaxy samples for which the masses and SFRs are inferred invidually for every galaxy. As discussed in Section 2, the determination and understanding of the SFR- $M_*$  relation and its evolution for MS galaxies can be affected due to i) intrinsic selection effects in large galaxy samples and ii) the comparison of SFRs based on different tracers and estimations is not trivial. In our approach, this is not the case since the evolution of the MS is derived from the FUV and IR LFs and the GSMF, distributions that are complete in volume, luminosities and mass over a large redshift range. Our main results are as follows:

- The homogeneously obtained SFRs as a function of  $M_*$  for redsfhits  $0 \lesssim z \lesssim 4$  confirm and unify, within the scatter, the values obtained previously from different galaxy surveys and using a diversity of SFR tracers and methodologies to estimate it, see Figure 4.
- Our methodology allows for consistent inferences of the mean sSFR-M\* relationships for MS galaxies down to low masses. Moreover, it allows for reliable extrapolations down to the regime of dwarf galaxies, where the unobscured FUV component dominates, Figures 5 and 7.
- The mean sSFR- $M_*$  relation for MS galaxies bends strongly at low masses and the slope sign changes from positive at low masses to negative at higher masses at all redshifts. The bending in the MS at lower masses is connected to the knee of the FUV LF, see Figure 6.
- At  $z \sim 0$  the change of sign in the MS occurs around  $M_* \sim 5 \times 10^8 {\rm M}_{\odot}$  which is close to the dust-obscured star formation regime at this redshift,  $M_* \sim 6 \times 10^8 {\rm M}_{\odot}$ .
- At  $z \sim 0$ , the resulting contributions from unobscured, FUV, and obscured, IR, SFRs are in good agreement with the results from the KINGFISH sample (based on GALEX and Herschel Space Observatory data) and the dust attenuation values  $A_{\rm FUV}$  reported in the GSWLC-2 (based on

GALEX, SDSS and WISE). At  $0.5 \lesssim z \lesssim 2.5$  we show that our results capture the observed trends to the contributions from FUV and IR to the total SFRs from Whitaker et al. (2014).

- At all redshifts the contribution from FUV dominates the total sSFR– $M_*$  relation at low masses, Figures 8 and 9. The characteristic mass for the obscured SFR regime has decreased a factor of  $\sim 3$  since  $z \sim 4$ :  $M_{*,\rm obsc} \sim 2 \times 10^9 {\rm M}_{\odot}$  at  $z \sim 4$  and  $M_{*,\rm obsc} \sim 6 \times 10^8 {\rm M}_{\odot}$  at  $z \sim 0$ , see Figure 10.
- The fraction of obscured SFR, SFR<sub>IR</sub>/SFR<sub>FUV+IR</sub>, depends strongly on mass and it changes very little with redshift for z>1.2, in agreement with Tomczak et al. 2016; Whitaker et al. 2017, Figure 9. Below  $z\sim0.75$ , galaxies more massive than  $\sim10^{10}~\rm M_{\odot}$  become more "transparent" than their high-redshift counter parts, while for low-mass galaxies, the opposite is true as they become more obscured by dust, see Figure 9.

According to our results, the sSFR- $M_*$  relation bends and changes its slope sign from positive at low masses to negative at high masses. At  $z \sim 0$ , this change occurs at  $M_* \sim 5 \times 10^8 {\rm M}_{\odot}$ . This has interesting implications for dwarfs galaxies. If we interpret the inverse of the total sSFR as the characteristic time that it will take a galaxy to double its mass at a constant SFR, then the above implies that dwarf MS galaxies,  $M_* \lesssim 5 \times 10^8 \mathrm{M}_{\odot}$ , form stars at a lower pace than intermediate mass MS galaxies,  $10^9 \lesssim M_*/\mathrm{M}_{\odot} \lesssim 10^{10}$ . For our low mass limit of  $M_* \sim 7 \times 10^7 \mathrm{M}_{\odot}$ , we find that sSFR  $\sim 10^{-10} \mathrm{yr}^{-1}$ , see Figure 7. Assuming a constant SFH, this implies an assembling time of  $\sim 10$  Gyrs. Observations of nearby dwarf galaxies show a significant mass fraction,  $\gtrsim 30\%$ , in stellar populations older than 10-11 Gyr (Weisz et al. 2014), consistent with our estimation. Note that if the sSFR of low-mass galaxies would follow the same trend with  $M_*$  as the one for  $M_* \gtrsim 10^9 {\rm M}_{\odot}$ , then the assembling time would be of  $\lesssim 2$  Gyr. That is, dwarf galaxies would be just in their process of formation, in clear disagreement with our results and with the resolved SFHs from nearby dwarf galaxies.

There are other observational works of local starforming dwarf galaxies that also show that their mean sSFR- $M_*$  relation bends with respect to the MS at higher masses (e.g., McGaugh et al. 2017; Davies et al. 2019). However, in these works the slope of the low-mass MS is not as steep as in our case, though this is difficult to evaluate the scatter of the MS increases at lower masses (see e.g., Davies et al. 2019). Motivated by the above, we have repeated our calculations at  $z \sim 0$  by increasing the scatter only for the FUV contribution from  $0.3~{\rm dex}$  to  $0.5~{\rm dex}$  (recall that for low-mass galaxies the FUV is more important). We find that the slope at low masses of the resulting mean sSFR– $M_*$  relation becomes slightly shallower as compared to the results based on the dispersion of  $0.3~{\rm dex}$ . More accurate observational studies of low-mass and in particular of dwarf galaxies will be key to confirm the bend of the mean sSFR– $M_*$  relation.

Studying the joint evolution of the FUV and IR restframe LFs and the GSMF appears as a promising and powerful approach to understand the contribution of unobscured (FUV) and obscured (IR) to the total SFRs as a function  $M_*$  and z, and ultimately to constrain models of the formation and destruction of dust in galaxies. Our results indicate that there seems to be a feedback mechanism between the presence of dust and the star formation activity. The increase of heavy element abundances, and hence of the dust content, is a direct result of the star forming activity. For high-mass galaxies at their early stages of evolution, the vigorous star forming activity supplies the ambient interstellar medium with a generous amount of recently formed dust. This may provide the required opacity to shield the neighbouring gas from the stellar UV radiation (e.g., Franco & Cox 1986), stimulating the formation of a new generation of molecular clouds. This in turn induces the conditions for further star formation and the resulting luminosity evolution proceeds in a dust-obscured fashion. For the case of low mass galaxies, in contrast, with a milder star formation rate than their massive counterparts, the evolution proceeds at a slower rate with a slowly growing metal content and, hence, are correspondingly more transparent, this scenario will be explored in more detail in a future publication. However, it is not clear why the dust-obscured fraction evolves mostly below  $z \sim 1$  but there is little evolution between  $z \sim 1.5$  and  $z \sim 4$ . Perhaps our results indicate that the dust production and destruction is not the full story but the spatial distribution of dust and its dependence on disk secular evolution might play a relevant role (e.g., Dalcanton et al. 2004).

Future research should be focused on confirming whether the redshift evolution of the GSMF is consistent with the evolution of FUV and IR LFs. Here we found some hints that this could be the case, by being in agreement with the observed trends of the sSFR- $M_*$  relationship and the dust-obscured fraction results obtained directly from galaxy surveys. Extending the semi-empirical modelling like those presented in Rodríguez-Puebla et al. (2017); Moster et al. (2018); Tacchella et al. (2018) and Behroozi et al. (2019) to include FUV and IR LFs looks very promising and timely to understand how dark matter halos build their stel-

lar mass and the evolution of dust in their host galaxies (Rodríguez-Puebla et al. in prep.). In addition, more theoretical work will be needed in order to understand the role of the dust and the trends with the fraction of obscured SFR derived here.

#### ACKNOWLEDGMENTS

ARP and VAR acknowledge support from UNAM PA-PIIT grant IA104118 and from the CONACyT 'Ciencia Basica' grant 285721. This project makes use of the MaNGA-Pipe3D dataproducts. We thank the IA-UNAM MaNGA team for creating this catalogue, and the CONACYT-180125 project for supporting them

### **APPENDIX**

### A. THE GSMF

We define the GSMF as the sum of two modified Schechter components,  $\phi_* = \phi_{*,1} + \phi_{*,2}$ :

$$\phi_{*,i}(M_*) = \phi_i^* \left(\frac{M_*}{M_i}\right)^{1+\alpha_i} \exp\left[-\left(\frac{M_*}{M_i}\right)^{\beta_i}\right],\tag{A1}$$

we assume that  $\beta_1=1$ ,  $\phi_2=6\times\phi_1$ ,  $M=M_1=M_2$  and that  $\alpha_2=1+\alpha_1$ . The above guarantees that the first component is a Schechter function while the second component is a modified Schechter component dominating the massive-end,  $M_*\gtrsim M_i$ , of the GSMF. Similarly to the LF we integrate our mass function over the redshift range that the GSMF is being observed:  $\phi_{\rm obs}(z_i,z_f)=\int \phi_*(z)dV(z)/(V_i-V_f)$ . The best fitting models to the compilation from Rodríguez-Puebla et al. (2017) are:

$$\alpha(z) = (-1.758 \pm 0.026) + \log(\mathcal{Q}(z; 2.123 \pm 0.187, 0, 2.815 \pm 0.297)), \tag{A2}$$

$$\phi(z) = (-3.161 \pm 0.070) + \log(\mathcal{Q}(z; 2.538 \pm 0.252, 0, 1.472 \pm 0.183)), \tag{A3}$$

$$M(z) = (-10.204 \pm 0.118) + \log(\mathcal{Q}(z; 6.961 \pm 0.423, -0.338 \pm 0.139, 5.529 \pm 0.229)),$$
 (A4)

and

$$\beta = 0.611 \pm 0.037. \tag{A5}$$

Figure 11 compares our the best fitting model with observations. Finally, in order to compute the GSMF of SFGs we use the fraction of SFGs from Rodríguez-Puebla et al. (2017) described in their Section 4.4.

### REFERENCES

Alavi, A., Siana, B., Richard, J., et al. 2014, ApJ, 780, 143, doi: 10.1088/0004-637X/780/2/143

—. 2016, ApJ, 832, 56, doi: 10.3847/0004-637X/832/1/56 Arnouts, S., Schiminovich, D., Ilbert, O., et al. 2005, ApJL,

Arnouts, S., Schiminovich, D., Ilbert, O., et al. 2005, ApJL 619, L43, doi: 10.1086/426733

Atek, H., Richard, J., Kneib, J.-P., & Schaerer, D. 2018, MNRAS, 479, 5184, doi: 10.1093/mnras/sty1820

Behroozi, P., Wechsler, R. H., Hearin, A. P., & Conroy, C. 2019, MNRAS, 488, 3143, doi: 10.1093/mnras/stz1182

Béthermin, M., Doré, O., & Lagache, G. 2012, A&A, 537, L5, doi: 10.1051/0004-6361/201118607 Bhatawdekar, R., Conselice, C. J., Margalef-Bentabol, B., & Duncan, K. 2019, MNRAS, 486, 3805,

doi: 10.1093/mnras/stz866

Bouché, N., Dekel, A., Genzel, R., et al. 2010, ApJ, 718, 1001, doi: 10.1088/0004-637X/718/2/1001

Bouwens, R. J., Illingworth, G. D., Franx, M., & Ford, H. 2007, ApJ, 670, 928, doi: 10.1086/521811

Bouwens, R. J., Illingworth, G. D., Oesch, P. A., et al. 2011, ApJ, 737, 90, doi: 10.1088/0004-637X/737/2/90

—. 2012, ApJ, 754, 83, doi: 10.1088/0004-637X/754/2/83

—. 2015, ApJ, 803, 34, doi: 10.1088/0004-637X/803/1/34

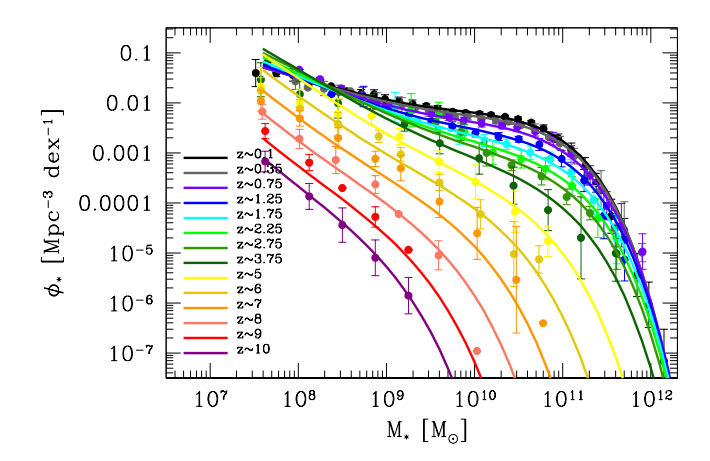


Figure 11. Best fitting model to the redshift evolution of the GSMF from Rodríguez-Puebla et al. (2017).

Brinchmann, J., Charlot, S., White, S. D. M., et al. 2004, MNRAS, 351, 1151, doi: 10.1111/j.1365-2966.2004.07881.x

Burgarella, D., Buat, V., Gruppioni, C., et al. 2013, A&A, 554, A70, doi: 10.1051/0004-6361/201321651

Cano-Díaz, M., Ávila-Reese, V., Sánchez, S. F., et al. 2019, MNRAS, 488, 3929, doi: 10.1093/mnras/stz1894

Cano-Díaz, M., Sánchez, S. F., Zibetti, S., et al. 2016, ApJL, 821, L26, doi: 10.3847/2041-8205/821/2/L26

Casey, C. M., Berta, S., Béthermin, M., et al. 2012, ApJ, 761, 140, doi: 10.1088/0004-637X/761/2/140

Chabrier, G. 2003, PASP, 115, 763, doi: 10.1086/376392

Conselice, C. J., Wilkinson, A., Duncan, K., & Mortlock, A. 2016, ApJ, 830, 83, doi: 10.3847/0004-637X/830/2/83

Cucciati, O., Tresse, L., Ilbert, O., et al. 2012, A&A, 539, A31, doi: 10.1051/0004-6361/201118010

Dalcanton, J. J., Yoachim, P., & Bernstein, R. A. 2004, ApJ, 608, 189, doi: 10.1086/386358

Davé, R., Finlator, K., & Oppenheimer, B. D. 2012, MNRAS, 421, 98, doi: 10.1111/j.1365-2966.2011.20148.x

Davies, L. J. M., Lagos, C. d. P., Katsianis, A., et al. 2019, MNRAS, 483, 1881, doi: 10.1093/mnras/sty2957

Driver, S. P., Robotham, A. S. G., Kelvin, L., et al. 2012, MNRAS, 427, 3244,

doi: 10.1111/j.1365-2966.2012.22036.x

Driver, S. P., Andrews, S. K., da Cunha, E., et al. 2018, MNRAS, 475, 2891, doi: 10.1093/mnras/stx2728

Duncan, K., Conselice, C. J., Mortlock, A., et al. 2014, MNRAS, 444, 2960, doi: 10.1093/mnras/stu1622

Eser, E. K., Goto, T., & Doi, Y. 2017, Publication of Korean Astronomical Society, 32, 299, doi: 10.5303/PKAS.2017.32.1.299

Fang, J. J., Faber, S. M., Koo, D. C., et al. 2018, ApJ, 858, 100, doi: 10.3847/1538-4357/aabcba Finkelstein, S. L., Ryan, Jr., R. E., Papovich, C., et al. 2015, ApJ, 810, 71, doi: 10.1088/0004-637X/810/1/71
Franco, J., & Cox, D. P. 1986, PASP, 98, 1076, doi: 10.1086/131876

González, V., Labbé, I., Bouwens, R. J., et al. 2011, ApJL, 735, L34, doi: 10.1088/2041-8205/735/2/L34

Gruppioni, C., Pozzi, F., Rodighiero, G., et al. 2013, MNRAS, 432, 23, doi: 10.1093/mnras/stt308

Hathi, N. P., Ryan, R. E., J., Cohen, S. H., et al. 2010, ApJ, 720, 1708, doi: 10.1088/0004-637X/720/2/1708

Ilbert, O., Arnouts, S., Le Floc'h, E., et al. 2015, A&A, 579, A2, doi: 10.1051/0004-6361/201425176

Karim, A., Schinnerer, E., Martínez-Sansigre, A., et al. 2011, ApJ, 730, 61, doi: 10.1088/0004-637X/730/2/61

Kennicutt, Robert C., J. 1998, ARA&A, 36, 189, doi: 10.1146/annurev.astro.36.1.189

Le Floc'h, E., Papovich, C., Dole, H., et al. 2005, ApJ, 632, 169, doi: 10.1086/432789

Lee, N., Sanders, D. B., Casey, C. M., et al. 2015, ApJ, 801, 80, doi: 10.1088/0004-637X/801/2/80

Lim, C.-F., Wang, W.-H., Smail, I., et al. 2020, ApJ, 889, 80, doi: 10.3847/1538-4357/ab607f

Livermore, R. C., Finkelstein, S. L., & Lotz, J. M. 2017, ApJ, 835, 113, doi: 10.3847/1538-4357/835/2/113

Madau, P., & Dickinson, M. 2014, ARA&A, 52, 415, doi: 10.1146/annurev-astro-081811-125615

Magnelli, B., Elbaz, D., Chary, R. R., et al. 2011, A&A, 528, A35, doi: 10.1051/0004-6361/200913941

Magnelli, B., Popesso, P., Berta, S., et al. 2013, A&A, 553, A132, doi: 10.1051/0004-6361/201321371

McGaugh, S. S., Schombert, J. M., & Lelli, F. 2017, ApJ, 851, 22, doi: 10.3847/1538-4357/aa9790

Mehta, V., Scarlata, C., Rafelski, M., et al. 2017, ApJ, 838, 29, doi: 10.3847/1538-4357/aa6259

- Moster, B. P., Naab, T., & White, S. D. M. 2018, MNRAS, 477, 1822, doi: 10.1093/mnras/sty655
- Murphy, E. J., Condon, J. J., Schinnerer, E., et al. 2011, ApJ, 737, 67, doi: 10.1088/0004-637X/737/2/67
- Muzzin, A., Marchesini, D., Stefanon, M., et al. 2013, ApJ, 777, 18, doi: 10.1088/0004-637X/777/1/18
- Noeske, K. G., Weiner, B. J., Faber, S. M., et al. 2007, ApJL, 660, L43, doi: 10.1086/517926
- Oesch, P. A., Bouwens, R. J., Carollo, C. M., et al. 2010, ApJL, 725, L150, doi: 10.1088/2041-8205/725/2/L150
- Oesch, P. A., Bouwens, R. J., Illingworth, G. D., et al. 2012, ApJ, 759, 135, doi: 10.1088/0004-637X/759/2/135
- Ono, Y., Ouchi, M., Harikane, Y., et al. 2018, PASJ, 70, S10, doi: 10.1093/pasj/psx103
- Pannella, M., Carilli, C. L., Daddi, E., et al. 2009, ApJL, 698, L116, doi: 10.1088/0004-637X/698/2/L116
- Parsa, S., Dunlop, J. S., McLure, R. J., & Mortlock, A. 2016, MNRAS, 456, 3194, doi: 10.1093/mnras/stv2857
- Popesso, P., Morselli, L., Concas, A., et al. 2019a, MNRAS, 490, 5285, doi: 10.1093/mnras/stz2635
- Popesso, P., Concas, A., Morselli, L., et al. 2019b, MNRAS, 483, 3213, doi: 10.1093/mnras/sty3210
- Reddy, N. A., Pettini, M., Steidel, C. C., et al. 2012, ApJ, 754, 25, doi: 10.1088/0004-637X/754/1/25
- Reddy, N. A., & Steidel, C. C. 2009, ApJ, 692, 778, doi: 10.1088/0004-637X/692/1/778
- Robotham, A. S. G., & Driver, S. P. 2011, MNRAS, 413, 2570, doi: 10.1111/j.1365-2966.2011.18327.x
- Rodighiero, G., Daddi, E., Baronchelli, I., et al. 2011, ApJL, 739, L40, doi: 10.1088/2041-8205/739/2/L40
- Rodríguez-Puebla, A., Avila-Reese, V., & Drory, N. 2013, ApJ, 767, 92, doi: 10.1088/0004-637X/767/1/92
- Rodríguez-Puebla, A., Primack, J. R., Avila-Reese, V., & Faber, S. M. 2017, MNRAS, 470, 651, doi: 10.1093/mnras/stx1172
- Salim, S., Boquien, M., & Lee, J. C. 2018, ApJ, 859, 11, doi: 10.3847/1538-4357/aabf3c
- Salim, S., Rich, R. M., Charlot, S., et al. 2007, ApJS, 173, 267, doi: 10.1086/519218
- Salim, S., Lee, J. C., Janowiecki, S., et al. 2016, ApJS, 227, 2, doi: 10.3847/0067-0049/227/1/2

- Salmon, B., Papovich, C., Finkelstein, S. L., et al. 2015, ApJ, 799, 183, doi: 10.1088/0004-637X/799/2/183
- Salpeter, E. E. 1955, ApJ, 121, 161, doi: 10.1086/145971
- Sánchez, S. F., Pérez, E., Sánchez-Blázquez, P., et al. 2016, RMxAA, 52, 171. https://arxiv.org/abs/1602.01830
- Sánchez, S. F., Avila-Reese, V., Hernandez-Toledo, H., et al. 2018, RMxAA, 54, 217.
  - https://arxiv.org/abs/1709.05438
- Santini, P., Fontana, A., Castellano, M., et al. 2017, ApJ, 847, 76, doi: 10.3847/1538-4357/aa8874
- Sargent, M. T., Béthermin, M., Daddi, E., & Elbaz, D. 2012, ApJL, 747, L31, doi: 10.1088/2041-8205/747/2/L31
- Schreiber, C., Pannella, M., Elbaz, D., et al. 2015, A&A, 575, A74, doi: 10.1051/0004-6361/201425017
- Shin, K., Ly, C., Malkan, M. A., et al. 2019, arXiv e-prints, arXiv:1910.10735. https://arxiv.org/abs/1910.10735
- Skibba, R. A., Engelbracht, C. W., Dale, D., et al. 2011, ApJ, 738, 89, doi: 10.1088/0004-637X/738/1/89
- Speagle, J. S., Steinhardt, C. L., Capak, P. L., & Silverman, J. D. 2014, ApJS, 214, 15, doi: 10.1088/0067-0049/214/2/15
- Tacchella, S., Bose, S., Conroy, C., Eisenstein, D. J., & Johnson, B. D. 2018, ApJ, 868, 92, doi: 10.3847/1538-4357/aae8e0
- Tomczak, A. R., Quadri, R. F., Tran, K.-V. H., et al. 2016, ApJ, 817, 118, doi: 10.3847/0004-637X/817/2/118
- van der Burg, R. F. J., Hildebrandt, H., & Erben, T. 2010, A&A, 523, A74, doi: 10.1051/0004-6361/200913812
- Weisz, D. R., Dolphin, A. E., Skillman, E. D., et al. 2014, ApJ, 789, 147, doi: 10.1088/0004-637X/789/2/147
- Whitaker, K. E., Pope, A., Cybulski, R., et al. 2017, ApJ, 850, 208, doi: 10.3847/1538-4357/aa94ce
- Whitaker, K. E., van Dokkum, P. G., Brammer, G., & Franx, M. 2012, ApJL, 754, L29, doi: 10.1088/2041-8205/754/2/L29
- Whitaker, K. E., Franx, M., Leja, J., et al. 2014, ApJ, 795, 104, doi: 10.1088/0004-637X/795/2/104
- Williams, R. J., Quadri, R. F., Franx, M., van Dokkum, P., & Labbé, I. 2009, ApJ, 691, 1879, doi: 10.1088/0004-637X/691/2/1879
- Wuyts, S., Labbé, I., Franx, M., et al. 2007, ApJ, 655, 51, doi: 10.1086/509708